Bounded Dark Energy

Giulia Borghetto[a, 1], Ameek Malhotra[a, 2], Gianmassimo Tasinato[a,b 3], Ivonne Zavala[a, 4]

[a] *Physics Department, Swansea University, SA2 8PP, UK*
[b] *Dipartimento di Fisica e Astronomia, Università di Bologna,*
INFN, Sezione di Bologna, I.S. FLAG, viale B. Pichat 6/2, 40127 Bologna, Italy

Recent cosmological observations suggest that the dark energy equation of state may have changed in the latter stages of cosmic history. We introduce a quintessence scenario, termed bounded dark energy, capable of explaining this feature in a technically natural way. Our approach is motivated from a bottom-up perspective, based on the concept of mirage cut-off, where we demonstrate the stability of the quintessence potential against large quantum corrections. At the same time, the bounded dark energy framework aligns well with top-down considerations motivated from quantum gravity arguments. We employ both human-driven insights and machine learning techniques to identify explicit realizations of bounded dark energy models. We then perform an analysis based on Markov Chain Monte-Carlo to assess their predictions against CMB, galaxy surveys, and supernova data, showing that bounded dark energy provides a good fit to current observations. We also discuss how upcoming measurements can further test and refine our proposal.

[1] giulia.borghetto@gmail.com
[2] ameek.malhotra@swansea.ac.uk
[3] g.tasinato2208@gmail.com
[4] e.i.zavalacarrasco@swansea.ac.uk

1 Motivations

Understanding the physics of dark energy remains one of the most pressing open problems in modern physics [1]. Numerous questions arise concerning the dark sector, both from observational and theoretical perspectives. Is dark energy dynamical? Why is its magnitude so small compared to theoretical expectations? Is there any mechanism to ensure stability of its properties against quantum corrections? We address some of these fundamental questions investigating quintessential potentials characterized by a scalar profile of the type depicted in Figure 1.

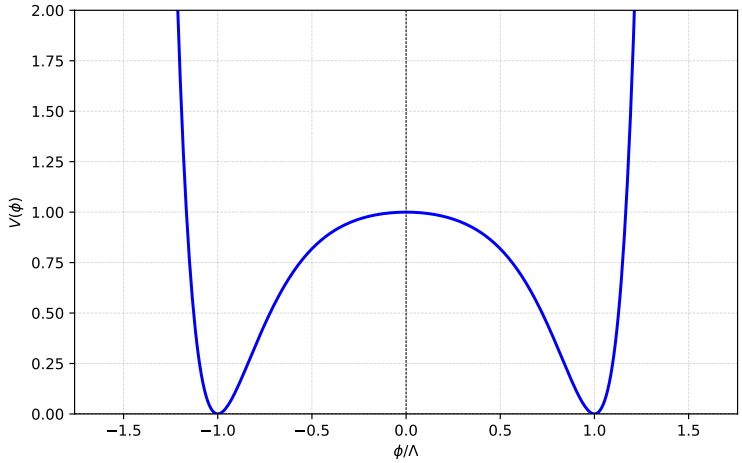

Figure 1. *The typical shape of a quintessence potential describing bounded dark energy scenarios.*

The quintessential scalar starts rolling from the local maximum of the potential, and its trajectory is bounded in field space by the steep growth of $V(\phi)$. Our reasons are the following:

1. Recent cosmological results [2–5] suggest that dark energy (DE) is dynamical.[5] Its behavior is well described by the so-called CPL parameterisation [41, 42], with a DE equation of state scaling as $w(z) = w_0 + w_a\, z/(1+z)$. In fact, analysis from the first year of observations from recent Baryon Acoustic Oscillation (BAO) surveys as well as recent Supernovae datasets reveal a marked preference for the CPL parameterization over LCDM [3, 4]. A dynamical DE following the CPL prescription crosses the phantom divide at $w = -1$, thus it is important to design theoretically consistent models avoiding such pathological behavior. Quintessence scenarios [43, 44], by construction, ensure that $w \geq -1$. Among this broad class of models, thawing quintessence [45] describes a setup where the scalar field begins to acquire significant

[5]The significance of these results, possibility of systematic effects and other different interpretations have been extensively discussed in [6–40].

kinetic energy relatively late during cosmic evolution. Such behavior typically occurs when the scalar initially evolves from a flat region of its potential (for example around a local maximum), which then steepens, leading to an increase in the scalar kinetic energy (see Fig. 1). The dynamics naturally lead to the condition $w_a < 0$ in the context of the CPL parameterization [46]. Consequently, thawing models are particularly relevant in light of current observational data. A notable example [6] is the class of hilltop quintessence models [49], for example recently studied in [48] in the context of string-motivated quintessence scenarios.

Moreover, quintessence potentials with sudden changes in their profile can effectively replicate accurately the dynamics of dark energy as described by the CPL parameterization, and at the same time avoid the phantom crossing divide: see e.g. [19, 22, 50, 51]. This leads us to explore models, as shown in Fig. 1, that exhibit particularly steep declines, following a flat region near the potential origin.

2. Thawing quintessence, based on a scalar field framework and hinted at by recent observations, introduces an additional layer of theoretical complexity for DE models. Not only must we explain why the DE scale is so small compared to other energy scales in particle physics [1], but we must also identify mechanisms to stabilize the distinctive shape of the scalar potential against quantum loop corrections. We aim to link the two problems and address them using the concept of *mirage cut-off* introduced in [52].

   The essential idea is that the scalar potential is constituted by a large number of contributions in its Taylor expansion, weighted by an overall small quantity:

$$V(\phi) = \epsilon \Lambda^4 \sum_{n=0}^{\infty} \frac{c_n}{n!} \left(\frac{\phi^2}{\Lambda^2}\right)^n \tag{1.1}$$

   with Λ an energy scale, ϵ a very small number, and c_n order-one coefficients. In our context, Λ represents the model cut-off, and $V_0 = \epsilon\Lambda^4$ sets the dark energy (DE) scale, which by having a small ϵ is significantly suppressed with respect to the cut-off scale Λ^4 (a small DE scale is of course well motivated by observations). Thanks to the smallness of ϵ, the flat region of the potential remains *stable under quantum corrections* [52]. We explore these ideas in Section 2.1, applying them to DE, and discussing how generic potentials like (1.1) naturally lead to boundaries in field space excursions, thanks to the (unavoidable) steep rises in their magnitude at finite values of the scalar field. Besides developing simple representative models in Section 2.1, in Section 3.2 we use machine learning techniques to find realisations of bounded DE setup with the correct features to accurately fit current cosmological data.

[6] Besides hilltop, other scalar potentials can fit current data well. See e.g. [47, 48] for recent cosmological analysis of string motivated quintessence models.

From a top-down perspective, a sudden change in the potential and the emergence of boundaries in field space may signal the presence of topological objects, as predicted by the cobordism conjecture[7] [53–55]. These could manifest as interpolating domain walls between consistent, cobordant theories (or vacua) at a finite distance in both field space and spacetime, as recently discussed in [56].

3. Potentials as Fig. 1, resembling a Mexican hat-like shape, naturally find realisations in symmetry breaking field theory scenarios. When coupling the DE scalar to matter fields, such symmetry breaking pattern also provides a natural screening mechanism for fifth forces, by means of the symmetron mechanism of [57], while simultaneously suggesting intriguing possibilities for setting the scalar field's initial conditions. We outline these arguments in Section 2.3.

The previous theoretical ideas are realised in explicit bounded dark energy scenarios, that we compare against the most recent cosmological data in Section 3.

2 Theoretical model building

A dynamical dark energy, if supported by data, requires model building efforts for establishing setups which are theoretically under control. We consider hilltop quintessential potentials with sharp boundaries in field space, as the one pictorially represented in Fig. 1. We provide arguments in favor of the technical stability of such potentials under quantum corrections, building on [52].

2.1 A bottom-up perspective

We start by progressively developing arguments supporting the stability of potentials like those shown in Fig. 1 under loop corrections, using an effective field theory perspective. We link the reduced size of quantum loop corrections with the smallness of the DE scale. The essential ingredient we use is the concept of mirage cut-off [52] applied to DE scenarios.

The scalar potentials $V(\phi)$ we consider exhibit a relatively flat plateau with a height V_0 around the origin $\phi \sim 0$. This is followed by a steep decline in the potential amplitude at a finite value of the scalar field, which then transitions into a rapid increase and reaches values much greater than V_0. Examples are quintessence hilltop scenarios [49], being equipped by a local maximum around which the scalar starts slowly rolling with an almost constant energy density – mimicking a cosmological constant at early times. Then, the flat region nearby the maximum changes slope and becomes steep, making the scalar roll faster from

[7] The cobordism conjecture suggests that in any consistent theory of quantum gravity all allowed configurations must not carry any cobordism charge, implying that the cobordism group must be trivial (i.e., vanish).

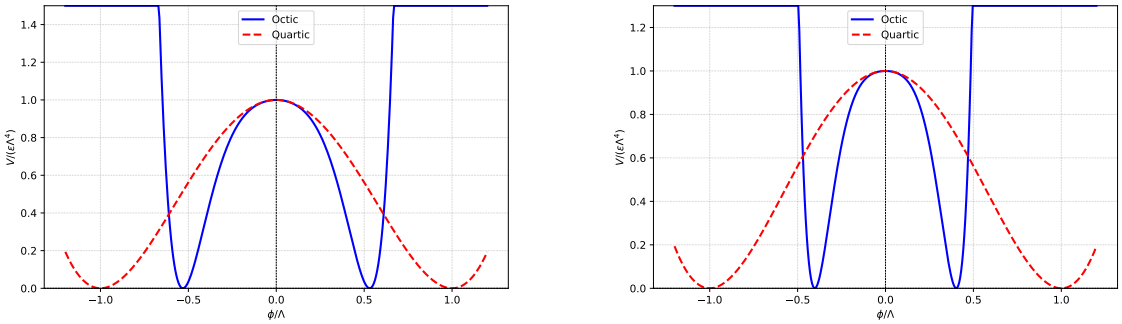

Figure 2. *Representation of the hilltop octic potential* (2.2) *(blue line), versus quartic potential* ($c_0 = 0$, *red dashed line).* **Left** $c_0 = 36$ **Right** $c_0 = 128$. *Larger values of* c_0 *make the potential descent steeper and steeper.*

a certain position onwards. A well-motivated, simple hilltop model is the quartic Higgs potential

$$V(\phi) \;=\; V_0 \left(1 - \frac{\phi^2}{\Lambda^2}\right)^2 , \tag{2.1}$$

tested for example in [48] against the most recent observational results. We proceed to analyse some of its possible generalizations.

The hilltop octic potential

We first consider a one-parameter extension of eq (2.1) examining the potential

$$V_{\rm oct}(\phi) \;=\; \epsilon\,\Lambda^4 \left(1 - \frac{\phi^2}{\Lambda^2} - \frac{c_0}{4}\,\frac{\phi^4}{\Lambda^4}\right)^2 . \tag{2.2}$$

We dub this potential *octic* since when expanding the parenthesis the scalar acquires powers up to level eight. In the limit $c_0 \to 0$ we recover the structure of quartic potential. The octic potential has a maximum at $\phi = 0$. The dimensionful quantity Λ, together with c_0, control the size of the flat region around the maximum of the potential. The value of the potential at the maximum is given by $V_0 = \epsilon\Lambda^4$. For our purposes of applying the system to DE, we consider very small values for ϵ, which enters as an overall factor of our potential. A quintessence model associated with potential (2.2) is not too sophisticated and it has not yet all the theoretically appealing features of the potentials we will consider next. Nevertheless it has the following interesting properties:

- First, the parameter c_0 can steepen the descending well of the potential compared to the quartic case, resulting in a more abrupt transition to the dynamical dark energy regime—see Fig. 2. The potential minimum is followed by a steep rise associated

with the large power ϕ^8. Sharp features and sudden transitions could have intriguing implications when confronted with recent findings in cosmological data sets. We develop this topic in Section 3.

- Second, potential (2.2) gives a first glance on the phenomenon of *mirage cut-off* [52]. Expanding (2.2), we observe that in the limit $\epsilon \ll 1$, the apparent cut-offs at levels six and eight in the expansion, $\epsilon^{-1/2}\,\Lambda$ and $\epsilon^{-1/4}\,\Lambda$, can be parametrically larger than the cut-off of the theory, of order Λ. If we were continuing the series with richer potentials, the size of the mirage cut-offs would become smaller and smaller, and approach Λ more and more. Such behavior can have interesting implications for the stability of the set-up under quantum corrections [52], as we are going to discuss next.

In fact, we now generalize the idea behind eq (2.2) and we pass to consider quintessence hilltop potentials made by an *infinite series* of powers of ϕ^2/Λ^2 terms, as

$$V(\phi) \,=\, \epsilon\,\Lambda^4 \sum_{n=0}^{\infty} \frac{c_n}{n!} \left(\frac{\phi^2}{\Lambda^2}\right)^n \,, \tag{2.3}$$

with c_n dimensionless coefficients of order one, and the overall coefficient ϵ a very small number, making the overall scale $V_0 \,=\, \epsilon\Lambda^4 \,\ll\, \Lambda^4$. The expansion (2.3) exhibits the phenomenon of mirage cut-off to which we alluded above [52]. The various terms exhibit cut-off scales scaling progressively as $\epsilon^{-1/2}\,\Lambda$, $\epsilon^{-1/4}\,\Lambda$, etc. Only probing the theory at high multiplicities of order $n > \ln \epsilon^{-1/2}$ the true cut-off of the theory, Λ, becomes manifest [52]. Hence we have the following chain of inequalities, controlled by the small ϵ:

$$\Lambda_{\rm DE} \,=\, \epsilon^{1/4}\,\Lambda \,\ll\, \Lambda \,\ll\, \epsilon^{-1/2}\,\Lambda \,=\, \Lambda_{\rm mirage} \tag{2.4}$$

where on the left is the DE scale (which we wish to be small). On the right the first mirage cut-off scale. In the middle, the true cut-off scale Λ of the theory, which can be probed at high multiplicities [8]. Inequality (2.4) makes clear that the smallness of ϵ is both related with the smallness of the DE scale and with the concept of mirage cut-off.

A peculiar feature of eq (2.3) is that it generally leads to pronounced features in the potential [52]. Since the coefficients c_n are of order one by hypothesis, the Taylor series converges, and defines an entire function in the complex plane. By Picard's Little Theorem, a non-constant entire function must assume all complex values, except possibly one. When restricted to the real domain, this feature implies that $V(\phi)$ will attain values much larger than V_0 for a finite $\bar{\phi}$ – at least of order Λ – effectively bounding the possible field excursions in a dynamical scalar setting. For the same reason, depending on the model and the signs

[8] In Section 2.2 we suggest ideas to realise scenarios with a small overall factor ϵ in front of the potential (2.3), by considering a geometrical, higher dimensional perspective to DE model building.

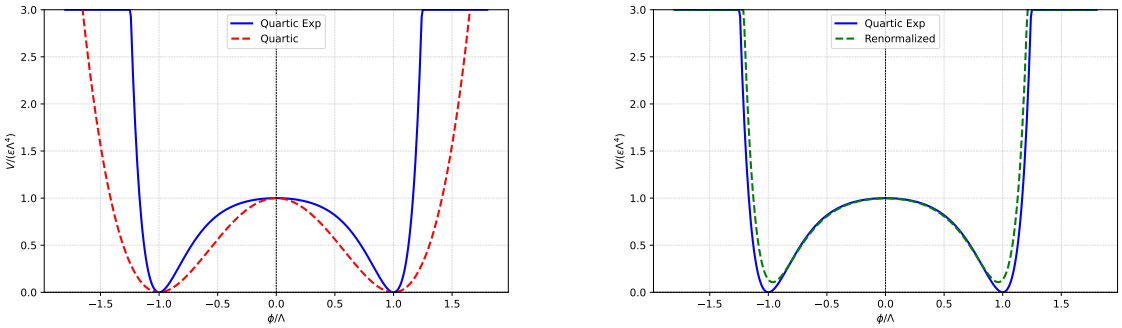

Figure 3. **Left panel**: *Representation of the hilltop exponential potential* (2.5) *against the quadratic case (blue* $\lambda = 1.5$*, dashed red* $\lambda = 0$*).* **Right panel**: *Hilltop exponential potential* (2.5) *(blue,* $\lambda = 1.5$*) against its renormalized version* (2.8) *(dashed green).*

of c_n, the potential $V(\phi)$ may also take values much smaller than V_0 for $\phi < \bar{\phi}$, possibly leading to local minima. See e.g. Fig. 1 for a possible realization.

The hilltop exponential potential

In order to be concrete, we consider examples where the infinite series (2.3) converges to known functions. We focus on a hilltop exponential potential [9]

$$V(\phi) = \epsilon \Lambda^4 \left(1 - \frac{\phi^2}{\Lambda^2}\right)^2 e^{\frac{\lambda \phi^2}{\Lambda^2}} \tag{2.5}$$

with the characteristics described above. Once expanded in a Taylor series, the potential takes the form (2.3). The dimensionless parameter λ in the exponent quantifies deviations from the quartic potential (with $\lambda = 0$). The small parameter ϵ controls the DE scale, see eq (2.4). The exponential correction to the quartic case introduces steep features in the potential, as illustrated in Fig. 3 (left panel), while also flattening it near the origin. The second derivative of the potential at $\phi = 0$ satisfies

$$\left.\frac{V''}{V}\right|_{\phi=0} = -\frac{2(2-\lambda)}{\Lambda^2}. \tag{2.6}$$

For $\lambda < 2$ – condition that we assume from now on – the potential has minima at $\phi = \pm\Lambda$, as in the quartic case. Beyond these minima, the potential grows steeply, halting any further field excursion, and giving rise to *bounded dark energy* scenario.

[9] This potential profile is based on a heuristic human guess. However, as we will learn in section 3.2, machine learning can achieve better results when theoretical arguments are applied to real data.

Stability of bounded DE potentials under loop corrections

From a theoretical perspective, an interesting property of the bounded DE model of eq (2.5) is that the potential shape is technically stable under quantum corrections, as shown in [52]. The idea exploits the smallness of the parameter ϵ, which is of course well motivated in a DE setup which requires a tiny value for the DE scale – see eq (2.4). The work [52] develops a regularization scheme for power-law divergences based on the true cut-off Λ of the theory as regularizing scale (which is much smaller than the mirage cut-off scale). Including power-law divergences only, we can work at linear order in the small parameter ϵ and include loop diagrams with a single insertion of the potential: [52] shows that the resulting renormalized potential at all loops is

$$V_{\rm ren}(\phi) = \frac{\sqrt{8\pi}}{\Lambda}\int_{-\infty}^{+\infty} d\tilde{\phi}\, e^{-\frac{8\pi^2(\tilde{\phi}-\phi)^2}{\Lambda^2}}\, V(\tilde{\phi})\,, \tag{2.7}$$

$$= \frac{\sqrt{2}\pi\,\epsilon\,\Lambda^4}{(8\pi^2-\lambda)^{5/2}}\, W(\phi) e^{\frac{8\pi^2\lambda\phi^2}{(8\pi^2-\lambda)\Lambda^2}}\,. \tag{2.8}$$

The first line (2.7) reports the general finding of [52], which we specialise in the second line (2.8) to our potential of eq (2.5) (under our hypothesis $\lambda < 2$). The function $W(\phi)$ is given by

$$W(\phi) = \frac{3}{2} + 128\pi^4 + 2\lambda + 2\lambda^2 - 16\pi^2(1+2\lambda) + \frac{128\pi^4(3-16\pi^2+2\lambda)}{(8\pi^2-\lambda)}\frac{\phi^2}{\Lambda^2} + \frac{8192\pi^8}{(8\pi^2-\lambda)^2}\frac{\phi^4}{\Lambda^4}\,. \tag{2.9}$$

We represent the renormalized potential in Fig. 3, right panel. Interestingly, the overall shape of the potential (2.5) is preserved: the flat region around the maximum at the origin is unchanged, as well as the initial potential descend, whereas the DE scalar becomes dynamical. Hence, appropriately regularized [52] power-law divergences do not spoil the properties of the quintessence potential. [10] This makes a dark energy quintessence scenario based on (2.5) technically natural from an effective field theory viewpoint. Only the minimum of the potential gets uplifted, from Minkowski to de Sitter [11].

Technically, the result (2.8) can be understood as a consequence of an approximate shift symmetry of the potential in the flat region around the maximum, which is broken by higher order terms in the potential which cause its rapid growth. Geometrically, such shift symmetry breaking is delocalized in field space away from the origin. Loop-induced power-law corrections are renormalized by regulators controlled by the *true* cut-off scale Λ

[10] We could also say this is called a *bounded DE scenario* because power-law loop corrections do not provide uncontrollable corrections to the scalar dynamics.

[11] This behavior has analogies with recent results on logarithmic loop corrections and de Sitter vacuua, as discussed in [58].

in this scenario. The procedure modifies the numerical coefficients in the expansion (2.3) by order-one factors, while preserving the overall structure of the potential. In particular, loop corrections involve higher derivatives, such as V''' and so on, which are suppressed when evaluated on the flat region near the origin. Therefore they do not affect the flatness of the potential at the local maximum, but only influence its features away from the origin.

2.2 The top-down viewpoint

From the top-down perspective, quantum gravity constraints on consistent theories of quantum gravity have been put forward in recent years in the form of a set of conjectures, which aim at delimiting the boundary between those EFT's which can be consistently UV completed – the landscape – and those which cannot – the swampland. Among such conjectures, one of the more relevant for cosmology, imposes constraints on the derivatives of the scalar potential, as the de Sitter conjecture [59, 60]. This conjecture demands that the scalar potential of the string moduli (describing sizes, shapes and positions in the extra dimensions, and the string coupling) arising from a compactification to four dimensions should satisfy [59, 60]:

$$\frac{\sqrt{\nabla^a V \nabla_a V}}{V} \geq \frac{c}{M_{\rm Pl}} \qquad \text{or} \qquad \frac{\min(\nabla^a \nabla_b V)}{V} \leq -\frac{c'}{M_{\rm Pl}^2}\,, \tag{2.10}$$

where "min()" denotes the minimal eigenvalue, and c and c' $\mathcal{O}(1)$ positive constants. Whilst there exist physical arguments for these inequalities to hold in asymptotic regions of the moduli space [60] – where large moduli correspond to weak couplings in the corresponding perturbative expansions – the conjecture speculates that it holds everywhere in moduli space. Conjecture (2.10) rules out a metastable de Sitter vacuum as the explanation for DE, as we can not have simultaneously $\nabla_a V = 0$, $V > 0$, and eigenvalues $(\nabla^a \nabla_b V) > 0$. On the other hand, recent cosmological data would also seem to indicate that a cosmological constant is not the source the current universe's accelerated expansion. The main alternative, from both theoretical and observational arguments, is possibly quintessence (see also [61]). Moreover, it is natural to expect that quintessence candidates are found amongst string moduli so long as their potential satisfies (2.10).

Potentials of the form (2.5) belong to the hilltop class and thus for suitable parameter values will satisfy the constraints (2.10). Concretely the quartic and octic potentials (2.1), (2.2) have $V_0''/V_0 = -4/\Lambda^2$ and thus for suitable Λ both satisfy (2.10) near the hilltop. The hilltop exponential, while having a more abrupt rise after the minimum, is flatter at the hilltop as seen from Fig. 3, with V_0''/V_0 given in (2.6). We shall discuss in Section 3.2 how we can use machine learning techniques with the theoretical input of the mirage cut-off to obtain examples of scalar potentials that score better in terms of the curvature at the hilltop.

We also point out that the abrupt rise of the potential at finite distances in field space

can have interesting relations with interpolating domain wall configurations arising in the context of the dynamical cobordism, as discussed in [56]. Mirage cut-offs may indicate non-trivial constraints on effective field theories, imposing a fundamental energy scale beyond which new physics must emerge.

Finally, string theory constructions can geometrically explain the smallness of the parameter ϵ in potentials of the form (2.3). For example, a small overall value for ϵ can arise from warping in moduli space, when identifying the scalar field with an axion in axion monodromy inflation [62]. We leave additional work on explicit string-motivated model building to future publications.

2.3 Symmetry breaking: screening mechanism and initial conditions

The bounded dark energy potentials discussed in Section 2.1 have a shape resembling symmetry-breaking, Mexican-hat configurations – see Fig. 1. We now discuss how such feature can be useful for a DE set-up, since it suggests ways to develop screening mechanisms, and to set initial conditions for the field dynamics when coupling the DE scalar to matter fields.

By promoting the scalar from a real to a complex field, we can write $\phi^2 = \Phi^\star \Phi$, and the potential becomes a deformed sombrero with a local maximum at the origin and a family of minima at vanishing potential, for values $\Phi = \bar{\phi} e^{i\varphi}$, with $\bar{\phi}$ the location of the minimum and φ an arbitrary phase. Concretely, the representative plot of Fig. 1 becomes a three-dimensional figure of revolution, representing a gauge symmetry breaking potential of the typical type considered in field theory setup.

In this context, long-range forces associated with the flat potential at the origin can be suppressed by means of a symmetron screening mechanism [57]. In essence, the symmetron mechanism hypothesizes that the field is also coupled to the energy density ρ of its environment, for example by a coupling proportional to $\rho|\Phi|^2$. When the energy density is large, the field is confined near $|\Phi| \simeq 0$ and acquires a large mass, rendering it unobservable in dense environments such as those on solar system scales, because it is unable to mediate long-range forces. In contrast, in a lower-density environment, the field moves toward its true minimum by rolling down its potential, and the DE dynamics takes place.

The very same idea can be used to theoretically motivate the initial conditions for the scalar field in our framework. To realise the thawing quintessence set-up and make DE dynamical, the scalar should start rolling around the tip of the hilltop potential. If, in the very early universe, the total energy density was large, a coupling proportional $\rho|\Phi|^2$ make the origin of the scalar potential a minimum instead of a maximum, initially keeping the scalar at that location. Only in more recent cosmological times, when ρ reduces its value, the effective scalar potential acquires the sombrero shape of Fig. 1, and the scalar starts rolling away from the origin.

The aforementioned ideas exploit the possibility that DE is coupled to dark matter and form an interacting DE-DM system. Couplings should be chosen appropriately to avoid

spoiling the stability of the setup under loop corrections, as discussed in Section 2.1. The realization of this system and the study of its phenomenology go beyond the scope of this work, and we leave them to a future publication.

3 Comparing with data

We now apply the theoretical considerations developed in the previous section using the most recent cosmological data. In Section 3.1, data will determine the best values for the parameters characterising the models analyzed in Section 2.1. Then, in Section 3.2 we employ machine learning techniques to refine the theoretical framework and leverage real data to identify the most compelling bounded dark energy scenarios.

To compare with observations, we modify the cosmological Boltzmann code `CAMB` [63] to implement the models described above. For each scenario, we explore the parameter space through a Markov Chain Monte-Carlo (MCMC) analysis. We vary three model specific parameters alongside the baseline cosmological parameters $\{\Omega_{\rm b}h^2, \Omega_{\rm c}h^2, H_0, \tau, A_s, n_s\}$, adopting wide uniform priors. The model parameter Λ is sampled in Planck units and H_0 in units of km/s/Mpc. We fix the overall potential amplitude to match the current dark energy scale. We use the following datasets:

1. CMB from *Planck*:
   - *Planck* 2018 low-ℓ temperature and polarisation likelihood [64].
   - *Planck* high-ℓ CamSpec TTTEEE temperature and polarization likelihood using `NPIPE` (*Planck* PR4) data [65].
   - *Planck* 2018 lensing likelihood [66].

   Hereafter, we collectively refer to all the *Planck* CMB likelihoods as 'CMB'.
2. BAO likelihoods from DESI DR1 [3, 67, 68]
3. Pantheon+ [69], Union3 [70] and DES-Y5 [2] type Ia supernovae likelihoods.

The choice of these datasets is based on the recent findings from the DESI BAO analysis [3], which suggests a preference for dynamical dark energy with relatively rapid evolution in the recent past, both independently and in combination with supernova datasets from Pantheon+ [69], Union3 [70] and DESY5 [2].

We employ the MCMC sampler [71, 72] in `Cobaya` [73]. The MCMC chains are considered to have converged when the Gelman-Rubin diagnostic satisfies the condition $R - 1 = 0.05$. To visualize the constraints and posterior distributions for each model, we use the `GetDist` package [74]. Additionally, we run the Scipy [75] minimizer via `Cobaya` to determine the maximum likelihood point and the corresponding χ^2 values. In Section 3.1 we present the results for the DE model parameters and the ΛCDM background parameters. The results for the full set of parameters can be found in Appendix A.

3.1 Comparing the models of section 2 against data

We now find the parameter values for the models of Section 2 which better fit current data.

Hilltop quartic Higgs potential

We start presenting the results for the hilltop quartic model analysed in [48], to better make the comparison between our hilltop models. The sampled parameters are Λ expressed in Planck units [12] and the initial relative field value ϕ_i/Λ, which represent the steepness of the potential and the initial displacement from the maximum, respectively. The results are shown in Figure 4, while Table 1 summarises the parameter means and the 68% limits. The resulting value of Λ is of the order of the Planck scale. As discussed previously in [48], we notice that for a steeper potential, i.e. a smaller Λ, the allowed values of ϕ_i/Λ are squeezed into a smaller region around the origin. Conversely, a shallower potential allows for a broader range but away from $\phi_i/\Lambda \approx 0$. This constraint arises to ensure the presence of dynamical dark energy in the present epoch, in particular for the CMB+DESI+DESY5 dataset shown in green. Note that in this case we varied two model parameters, whereas the octic and exponential hilltop models include an additional parameter (respectively c_0 and λ) that should also be sampled. The mean value for the cut-off Λ is of the order of the Planck scale, while the dark energy scale $V_0 = \epsilon\Lambda^4$ is around 120 orders of magnitude smaller. This in fact demonstrates that in our seup a small value for ϵ is very well motivated.

Parameter	**+Pantheon+**	**+Union3**	**+DESY5**
$\boldsymbol{\Lambda}$	> 1.29	> 1.24	> 1.17
$\boldsymbol{\phi_i/\Lambda}$	< 0.142	$0.151^{+0.073}_{-0.12}$	0.169 ± 0.081
$\boldsymbol{\Omega_c h^2}$	0.11838 ± 0.00082	0.11835 ± 0.00084	0.11829 ± 0.00084
$\boldsymbol{\Omega_b h^2}$	0.02228 ± 0.00012	0.02228 ± 0.00013	0.02228 ± 0.00013
$\boldsymbol{H_0}$	$67.29^{+0.59}_{-0.45}$	$66.7^{+1.0}_{-0.70}$	66.44 ± 0.64
ϕ_i	$0.174^{+0.071}_{-0.17}$	$0.235^{+0.088}_{-0.23}$	$0.26^{+0.10}_{-0.24}$

Table 1. Quartic hilltop model: parameter means and 68% limits for the addition of the different supernovae datasets to the CMB+DESI combination.

[12] From now on we use Planck units to express the cut-off value Λ.

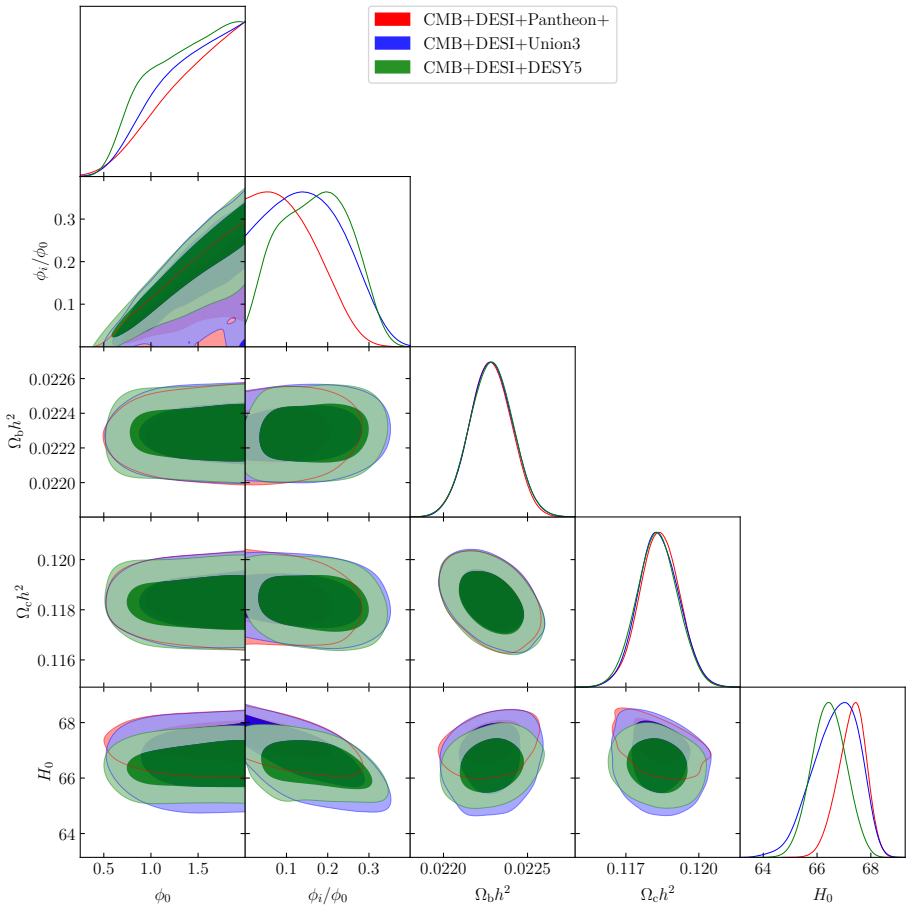

Figure 4. Constraints on the quartic Higgs hilltop model of eq (2.1) (68% and 95% contours).

Hilltop octic potential

For the octic model, we sample the parameters Λ, c_0 and ϕ_i/Λ. As before, ϕ_i/Λ represents the initial field displacement from the maximum, in units of Λ, while Λ and c_0 control the steepness of the potential. More specifically, larger values of c_0 and smaller values of Λ result in a steeper potential, and vice versa. The resulting parameter posterior distributions are plotted in Figure 5, with the 68% limits presented in Table 2. We learn that present data is unable to provide meaningful constraints on the parameter c_0, implying that the corresponding term in the scalar field potential does not play a significant role in the field evolution. Note however, that for larger c_0, a large initial field displacement ϕ_i/Λ is excluded (otherwise the potential becomes too steep). Given these considerations, it is not surprising that the ϕ_i/Λ vs Λ constraints resemble those of the quartic model. These features are also reflected in the three-dimensional scatter plot of the three parameters $c_0, \phi_i/\Lambda, \Lambda$, shown in Figure 6 for the CMB+DESI data in combination with Pantheon+ and DESY5.

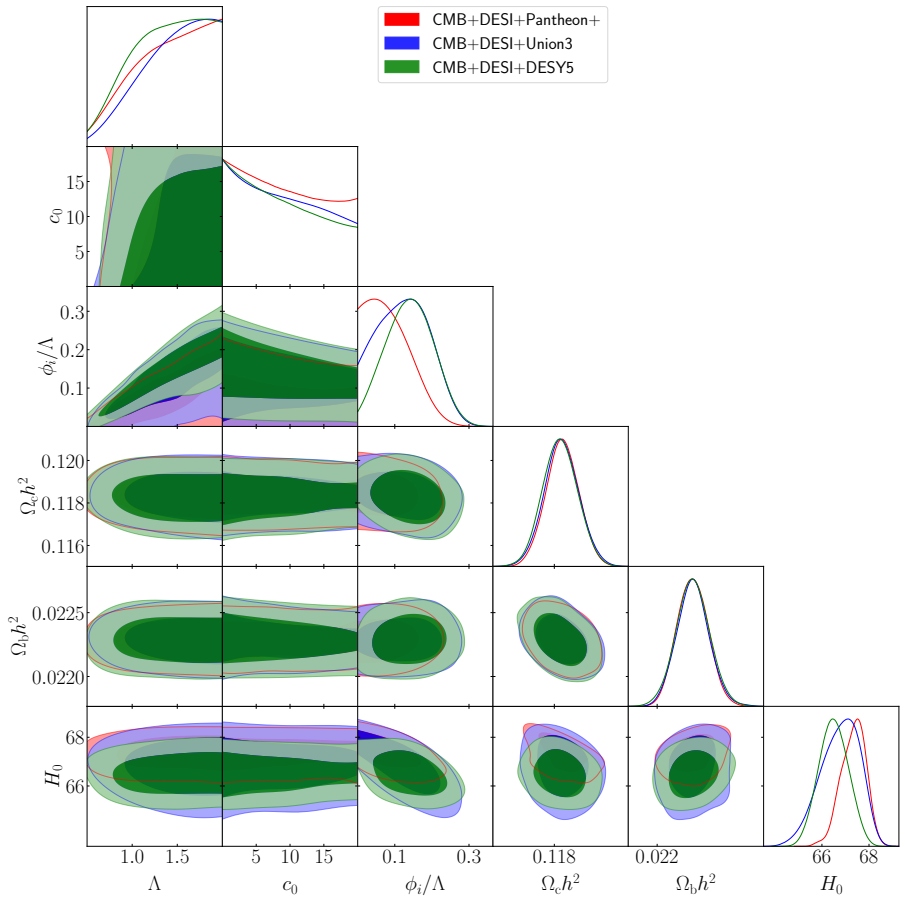

Figure 5. Parameter constraints (68% and 95% contours) for the hilltop octic model of eq (2.2).

Parameter	**+Pantheon+**	**+Union3**	**+DESY5**
$\boldsymbol{\Lambda}$	> 1.21	> 1.29	> 1.18
$\boldsymbol{c_0}$	—	< 12.4	< 11.8
$\boldsymbol{\phi_i/\Lambda}$	< 0.113	0.127 ± 0.067	0.141 ± 0.062
$\boldsymbol{\Omega_c h^2}$	0.11839 ± 0.00079	0.11835 ± 0.00084	0.11828 ± 0.00084
$\boldsymbol{\Omega_b h^2}$	0.02229 ± 0.00012	0.02229 ± 0.00013	0.02229 ± 0.00014
$\boldsymbol{H_0}$	$67.34^{+0.59}_{-0.47}$	$66.78^{+0.97}_{-0.70}$	66.50 ± 0.62
ϕ_i	$0.136^{+0.044}_{-0.14}$	$0.199^{+0.091}_{-0.17}$	$0.214^{+0.097}_{-0.17}$

Table 2. Hilltop octic model: parameter means and 68% limits for the addition of the different supernovae datasets to the CMB+DESI combination.

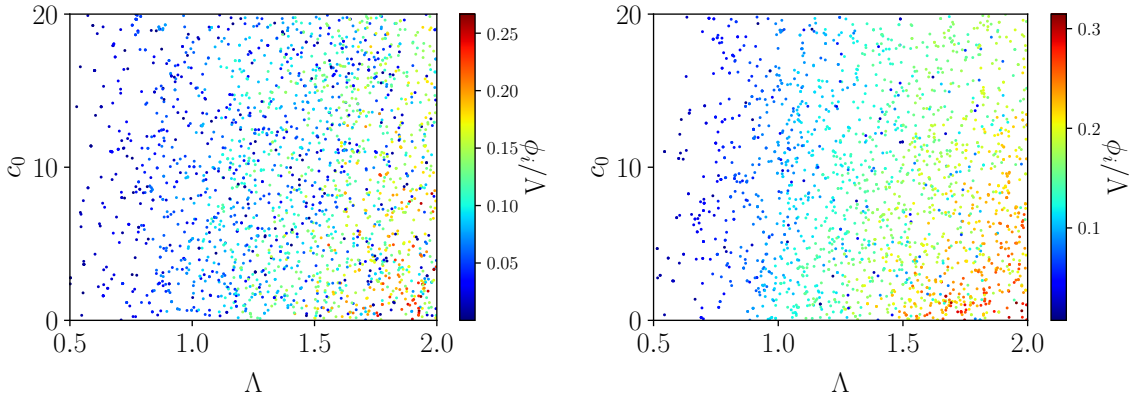

Figure 6. The DE model parameters $c_0, \phi_i/\Lambda, \Lambda$ plotted as a 3D scatter-plot generated from the MCMC samples for the octic model, using the CMB+DESI+Pantheon+ dataset (left) and CMB+DESI+DESY5 (right).

Hilltop exponential potential

For the hilltop exponential model, we vary the parameters Λ, λ and ϕ_i/Λ. The results are plotted in Figure 7 and the 68% limits presented in Table 3. Once again, we identify ϕ_i/Λ as the initial field displacement and we track the role of the other model parameters, λ and Λ, in controlling the steepness of the potential. Additionally, in this case, the parameter λ also influences the flatness of the potential around the origin, with bigger values resulting in a flatter area. This is reflected in the λ vs ϕ_i/Λ contours, where we learn that for larger λ (potential flatter at the origin), the initial field displacement can not be too small, in particular for the DESY5 dataset which requires the largest deviation from ΛCDM. A similar effect can be noticed in the λ vs Λ plot where one cannot have a potential flat at the hilltop as well as away from it for the same dataset, otherwise the late-time dark energy behavior resembles that of the cosmological constant. The ϕ_i/Λ vs Λ contours are interpreted similarly to the previous two potentials considered in this section. The 3-dimensional scatter plot of the three parameters $\lambda, \phi_i/\Lambda, \Lambda$, in Figure 8, reveal the same trends.

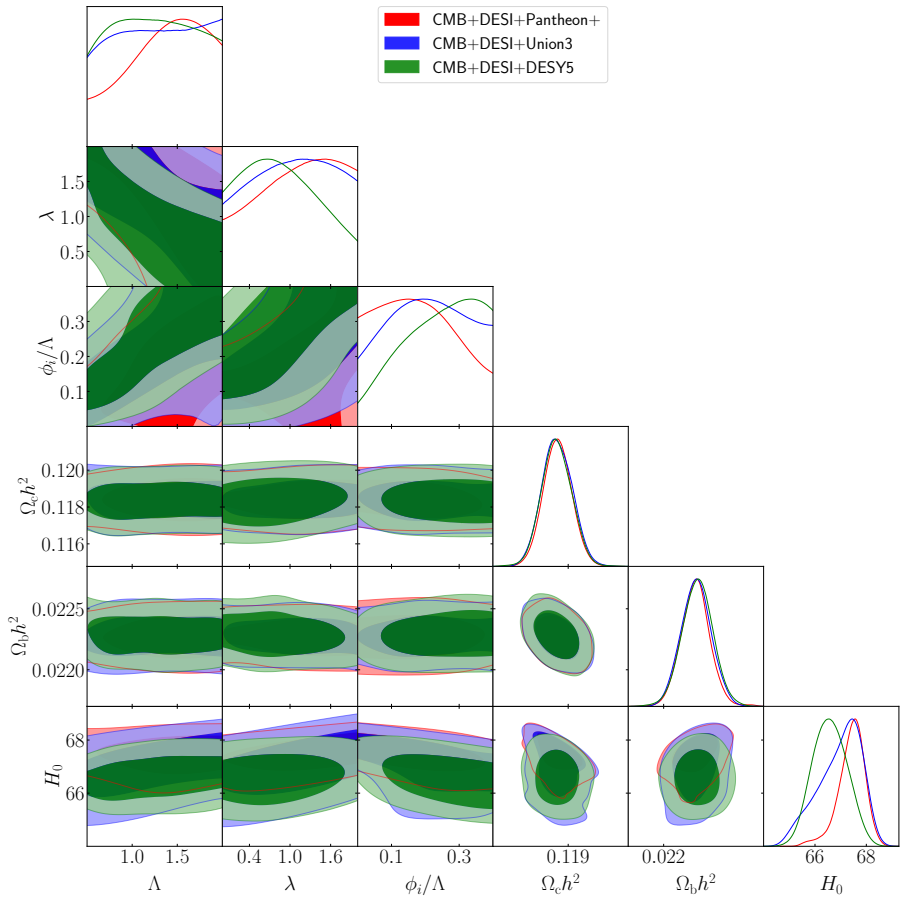

Figure 7. Parameter constraints (68% and 95% contours) for the hilltop exponential model of eq (2.5).

Parameter	+Pantheon+	+Union3	+DESY5
$\boldsymbol{\Lambda}$	$1.36^{+0.64}_{-0.20}$	—	—
$\boldsymbol{\lambda}$	> 0.823	—	$0.89^{+0.36}_{-0.80}$
$\boldsymbol{\phi_i/\Lambda}$	$0.180^{+0.068}_{-0.17}$	0.21 ± 0.11	> 0.183
$\boldsymbol{\Omega_c h^2}$	0.11840 ± 0.00079	0.11839 ± 0.00085	0.11835 ± 0.00085
$\boldsymbol{\Omega_b h^2}$	0.02227 ± 0.00013	0.02228 ± 0.00013	0.02229 ± 0.00013
$\boldsymbol{H_0}$	$67.42^{+0.57}_{-0.39}$	$67.0^{+1.1}_{-0.60}$	66.58 ± 0.67
ϕ_i	$0.25^{+0.10}_{-0.23}$	$0.28^{+0.12}_{-0.24}$	$0.31^{+0.14}_{-0.26}$

Table 3. Hilltop exponential model: parameter means and 68% limits for the addition of the different supernovae datasets to the CMB+DESI combination.

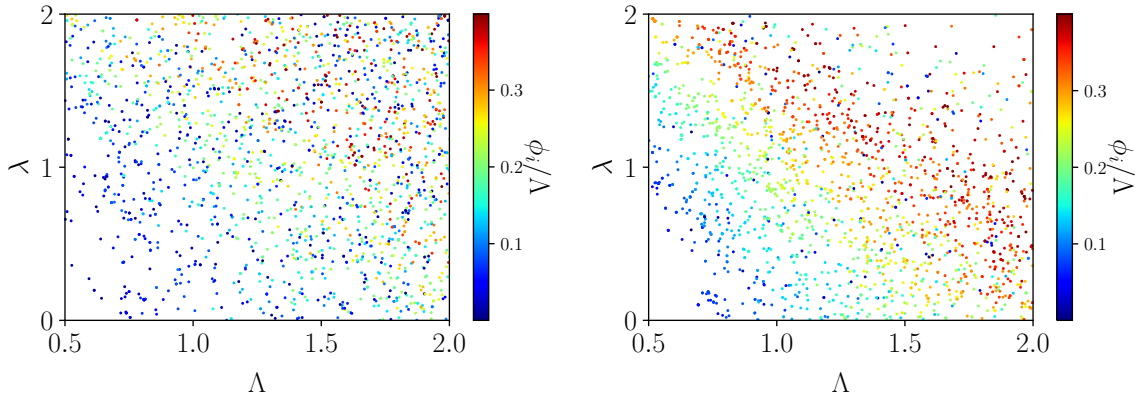

Figure 8. The DE model parameters $\lambda, \phi_i/\Lambda, \Lambda$ plotted as a 3D scatter-plot generated from the MCMC samples for the Hilltop Exponential model, using the CMB+DESI+Pantheon+ dataset (left) and CMB+DESI+DESY5 (right).

Summary of the results so far

In Fig. 9 we visualize some consequences of the results obtained so far, by plotting the evolution of the scalar field equation of state and the Hubble parameter as a function of redshift for the three models in this section. We compare these quantities with the DESI reconstruction using CMB+DESI+Union3 data [76], also representing the corresponding error bars. Our conclusions are as follows:

- The left panel in Fig. 9 indicates that the models are in the right track for reproducing the evolution of the DE equation of state as function of redshift, although they do not succeed in matching the DESI reconstruction exactly. The problem being that the shape of the potential must be tuned very precisely to allow for a scalar dynamics that better fits observations.

- Moreover, Tables 1-3 show that in the models considered so far the mean values of the cut-off scales Λ of the order of Planck scale. It would instead be desirable to find setup with a smaller cut-off scale, in order to ensure they are not destabilized by corrections involving graviton loops (more on this in Section 4).

To improve on these points, we now proceed using machine learning techniques to build bounded dark energy potentials starting from data themselves. Machine learning will be able to find bounded DE models with smaller cut-off scales, and which allow to better fit current observations.

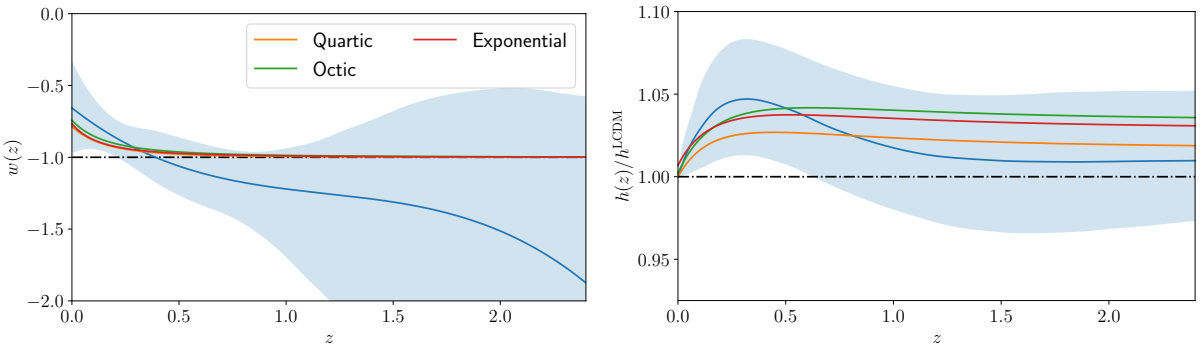

Figure 9. The evolution of $w_\phi(z)$ and $h(z) \equiv H(z)/H_0$ is shown for the best-fit hilltop models of section 3.1, and compared to the DESI reconstruction (blue line) using CMB+DESI+Union3 data [76]. The shaded regions represent the 95% confidence regions. As the CPL parametrization closely follows the DESI reconstruction, it is not plotted separately. At $z = 0$, $w_0 = -0.65$ for the reconstruction, while the values for the hilltop models are: $w_0 = -0.74$ for the octic model, $w_0 = -0.77$ for the exponential model, and $w_0 = -0.79$, for the quartic model. The best-fit parameter values for each model can be found in Appendix A.

3.2 A machine learning approach

The results of the previous Section 3.1 show that bounded DE scenarios can fit current observational data well, although they do not reconstruct DESI results as well as the CPL parametrization at low redshifts: see Fig. 9. It is interesting to apply machine learning (ML) techniques to reconstruct good examples of bounded DE potentials that better fit data, possibly with smaller values of the model cut-off.

We make use of techniques based on symbolic regression (SR), capable of identifying interpretable symbolic expressions that are translated into scalar potentials. The method balances prediction accuracy and model complexity. We aim to find a hilltop-type potential, in the same class of models studied in the theory Section 2, which mimic a cosmological constant at early times, while better capturing the steep rise of in the DESI reconstruction of $w(z)$ at low redshifts – see Fig. 9, blue line. For this purpose, as benchmark starting point, we consider a CPL-like model that never crosses the phantom divide at $w = -1$. We follow the example of [51], who reverse engineer $w(z)$ to find a potential. We start assuming $w = \max[-1, w_0 + w_a(1-a)]$, where $w_0 = -0.65$ and $w_a = -1.23$, which lead to the so-called ramp model in [51]. (The ramp potential $V_{\mathrm{RAMP}}(\phi)$ is represented in Fig. 10, left panel.) Taking inspiration from [77, 78], we then apply SR to regularize the potential features, and to determine a smooth hilltop potential symmetric around the origin, rapidly increasing at large values of ϕ.

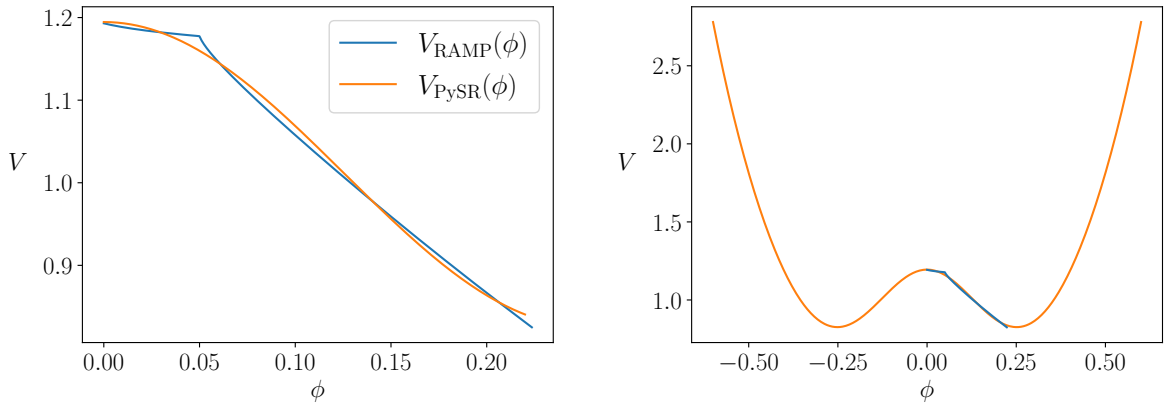

Figure 10. **Left panel:** PySR fit (orange line) of the ramp model of [51] (blue line). **Right panel:** Representation of the PySR potential (3.1) for a more extended interval of ϕ.

We use the Python package PySR [79] to explore the model space under a set of constraints on the allowed functional form for the desired scalar potential. We use the following set of operators $\{+, -, *, /, \text{power}, \exp\}$, and for simplicity we further restrict the search space by avoiding nested composition of operators, such as $e^{e^{e\phi}}$. In particular, we are interested in a generalization of the hilltop exponential potential (2.5). Therefore, we specify a custom template, $V_{\rm PySR}(\phi) = V_0\, e^{\lambda\,\phi^2/\Lambda^2} f(\phi^2)$, allowing PySR to determine the optimal form $f(\phi^2)$ and λ, i.e. the formula that optimally balances accuracy and simplicity [13].

Since PySR is an evolutionary algorithm, different runs can yield different expressions. Such behaviour is expected when considering the numerous possible combinations of the allowed operators, even under the constraints we imposed. We do however, note recurring patterns in the generated equations, which consistently approximate the ramp potential. We report a particularly well-performing result, which resembles the form of the hilltop models studied in this paper, and we test it against data, as in Section 3.1. The resulting potential is

$$V_{\rm PySR}(\phi) \;=\; V_0\, e^{0.01\,\phi^2/\Lambda^2} \left(a\,\frac{\phi^2}{\Lambda^2} + b + e^{c\phi^2/\Lambda^2} \right), \tag{3.1}$$

with best-fit coefficients $a = 0.04845719$, $b = 0.19458601$ and $c = -0.20447332$. We set $\Lambda = 0.1$ (well below the Planck scale), and V_0 at the value of the DE scale. As earlier, we express dimensionful quantities in Planck units. The potential is shown in Figure 10. In the left panel, we zoom the potential around the origin showing that it represents a smooth version of the ramp model of [51], without fully capturing its sharp feature occurring at $\phi \approx 0.06$. The reason being that a tighter fit of the ramp scenario would require a higher complexity of the expression, which is not rewarded by a much higher accuracy. Said this, as shown in Figure 11 the ML approach succeeds in reproducing a better trend of $w(z)$ at late times compared to the other hilltop models inspected in the previous sections.

[13] The corresponding codes are available upon request.

Figure 11 shows the evolution of $w(z)$ and $h(z)$, obtained using the results of a minimization process, conducted as in Section 3.1. Using the same datasets – CMB+DESI+Union3 [76] – we varied the usual baseline cosmological parameters $\{\Omega_b h^2, \Omega_c h^2, H_0, \tau, A_s, n_s\}$ along with a single additional parameter, ϕ_i, the initial position for the scalar field – see Appendix A for full results. Since we left SR to reconstruct the potential parameters from the data, we do not vary them. Hence, unlike the previous models, in this case the steepness of the potential is set by the best-fit values found by PySR.

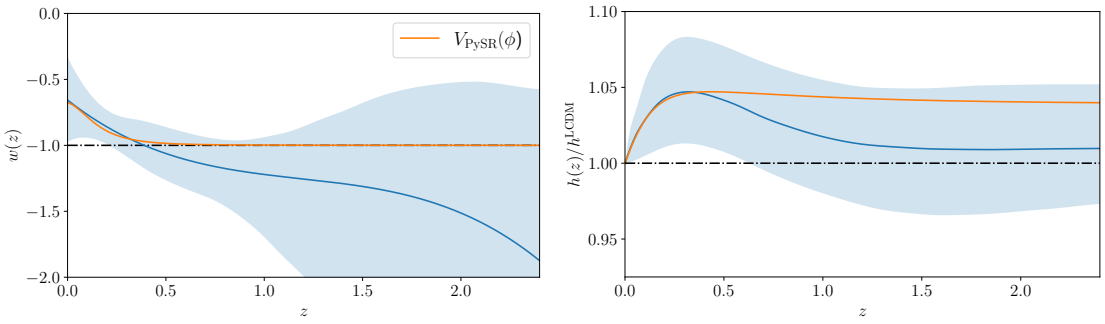

Figure 11. The figure shows the evolution of $w_\phi(z)$ and $h(z) \equiv H(z)/H_0$ for the potential determined by a ML method based on PySR, compared to the DESI reconstruction (blue line) using CMB+DESI+Union3 data [76]. At $z = 0$ we set $w_0 = -0.65$ and $w_0 = -0.68$ for the reconstruction and the best-fit hilltop model, respectively. The full set of best-fit parameters for $V_{\rm PySR}$ can be found in Appendix A.

To test how well the potential generated by PySR fits the data, we compute the $\Delta\chi^2$ comparing this model with ΛCDM, CPL, and the quartic, octic and exponential models of Section 2. The results for the CMB+DESI+Union3 combination are:

$$\Delta\chi^2_{\rm PySR} = \chi^2_{\rm PySR} - \chi^2_{\Lambda\rm CDM} = -4.6 \tag{3.2}$$
$$\Delta\chi^2_{\rm PySR} = \chi^2_{\rm PySR} - \chi^2_{\rm CPL} = 8.5 \tag{3.3}$$
$$\Delta\chi^2_{\rm PySR} = \chi^2_{\rm PySR} - \chi^2_{\rm quartic} = -2.2 \tag{3.4}$$
$$\Delta\chi^2_{\rm PySR} = \chi^2_{\rm PySR} - \chi^2_{\rm octic} = -2.1 \tag{3.5}$$
$$\Delta\chi^2_{\rm PySR} = \chi^2_{\rm PySR} - \chi^2_{\rm exp} = -1.4 \tag{3.6}$$

where $\chi^2 = -2\ln\mathcal{L}_{\rm max}$ for a given model. This shows that the ML model provides a better fit to the data compared to ΛCDM and the other hilltop potentials, although the phenomenological CPL parametrization remains the most favored scenario by data.

At the theory level, the ML potential (3.1) is interesting since it keeps the cut-off scale Λ well smaller than the Planck scale. Additionally, it satisfies better the swampland de Sitter conjecture inequalities (2.10) with respect to the other, human-generated models, suggesting once more that such inequalities are motivated by observational results.

4 Outlook

Recent data indicate that dark energy is dynamical. If so, it is crucial to develop well-controlled theoretical models to understand its nature. Motivated by these facts, we presented a model of hilltop quintessence dubbed bounded dark energy, characterized by a potential which exhibits a hilltop that appears relatively flat compared to its steep growth for large values of ϕ. We demonstrated that such potentials align closely with the recent proposal of theories characterized by a mirage cut-off [52]. We provided arguments supporting the stability of the quintessence potential against large quantum corrections. Additionally, we explored how bounded dark energy models naturally fit within top-down quantum gravity frameworks. Furthermore, we presented general considerations indicating that our hilltop scenarios can exhibit screening mechanisms and proposed methods for selecting appropriate initial conditions for the scalar field.

We presented simple, explicit examples of bounded dark energy models, confronting them with the most recent cosmological data sets. Although the model predictions are in reasonably good agreement with observations, we identified aspects that could be improved. Accordingly, we employed a machine learning approach for designing bounded dark energy potentials that are more consistent with observational results. We have shown that the resulting models fit data very well.

It will be interesting to further refine our understanding of bounded dark energy scenarios. While we focused on loop corrections associated with DE scalar field, it would be interesting to also consider the effects of graviton loops. If the model cut-off Λ is much smaller than the Planck scale, hopefully such graviton loops provide only negligible corrections. It would also be interesting to further refine the machine learning methods to build new potentials with parameters accommodating future observational results, and additionally imposing more stringent and well motivated theoretical priors for the shape of quintessential potentials.

Acknowledgments

We thank Sukannya Bhattacharya, Carlos Núñez and Susha Parameswaran for discussions on related topics. We are partially funded by the STFC grants ST/T000813/1 and ST/X000648/1. We also acknowledge the support of the Supercomputing Wales project, which is part-funded by the European Regional Development Fund (ERDF) via Welsh Government. For the purpose of open access, the authors have applied a Creative Commons Attribution licence to any Author Accepted Manuscript version arising. Research Data Access Statement: No new data were generated for this manuscript.

A Full parameter space constraints

In this section, we provide the plots and tables containing the complete set of parameters for the three hilltop models and for the symbolic regression model, as discussed in the main text. The results for the Hilltop quartic Higgs potential are obtained from [48].

Hilltop quartic Higgs potential

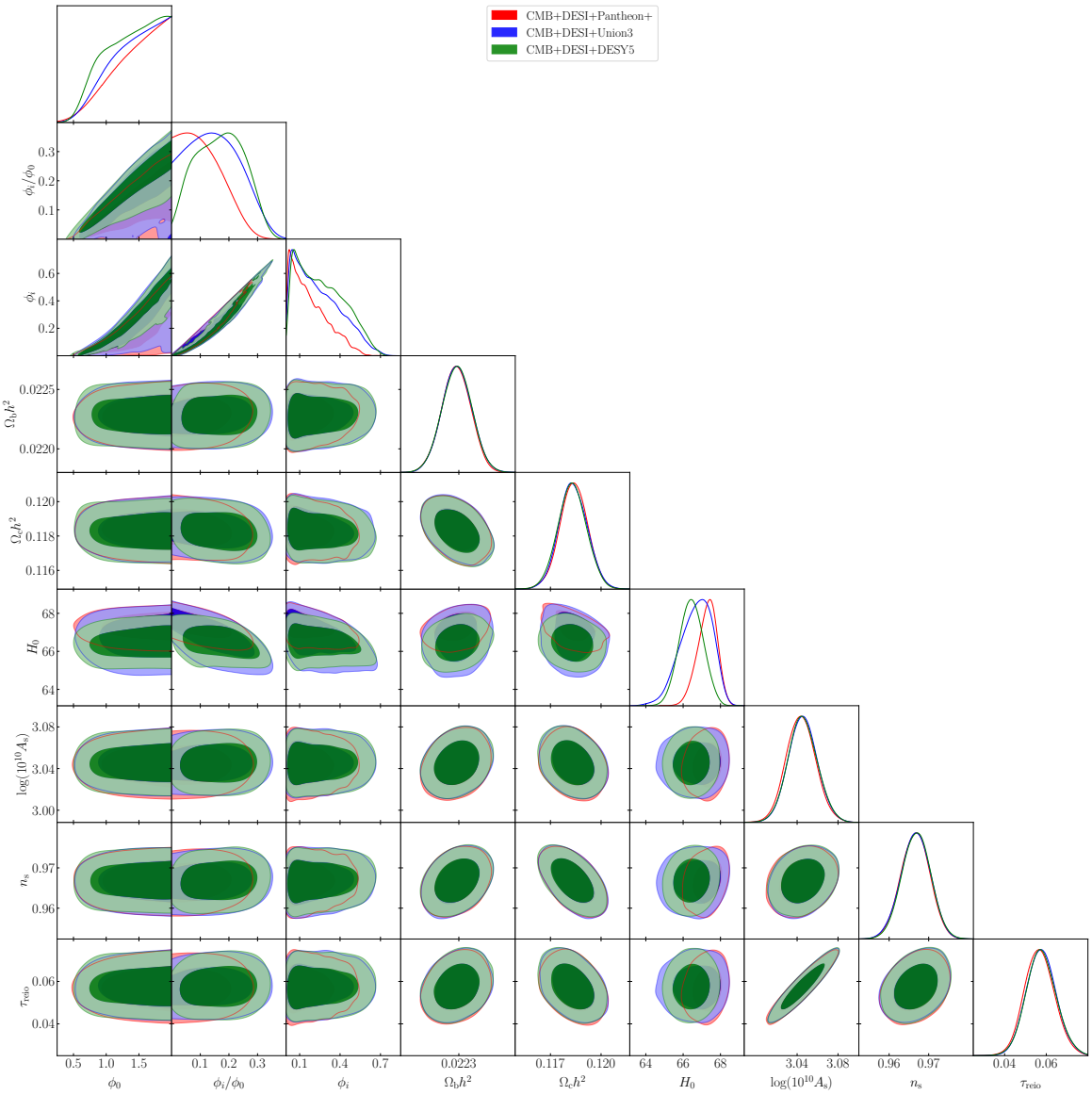

Figure 12. Full parameter constraints for the hilltop quartic model.

Parameter	+Pantheon+	+Union3	+DESY5
$\boldsymbol{\Lambda}$	> 1.29 (1.23)	> 1.24 (0.69)	> 1.17 (0.62)
$\boldsymbol{\phi_i/\Lambda}$	< 0.142 (0.106)	$0.151^{+0.073}_{-0.12}$ (0.051)	0.169 ± 0.081 (0.034)
$\boldsymbol{\Omega_c h^2}$	0.11838 ± 0.00082 (0.1188)	0.11835 ± 0.00084 (0.1176)	0.11829 ± 0.00084 (0.1189)
$\boldsymbol{\Omega_b h^2}$	0.02228 ± 0.00012 (0.02221)	0.02228 ± 0.00013 (0.00223)	0.02228 ± 0.00013 (0.02223)
$\boldsymbol{\log(10^{10} A_s)}$	3.044 ± 0.014 (3.041)	3.046 ± 0.014 (3.044)	3.045 ± 0.014 (3.033)
$\boldsymbol{n_s}$	0.9666 ± 0.0036 (0.9641)	0.9667 ± 0.0037 (0.9694)	0.9669 ± 0.0036 (0.9645)
$\boldsymbol{H_0}$	$67.29^{+0.59}_{-0.45}$ (66.98)	$66.7^{+1.0}_{-0.70}$ (66.30)	66.44 ± 0.64 (66.06)
$\boldsymbol{\tau_{reio}}$	0.0567 ± 0.0071 (0.0555)	0.0576 ± 0.0071 (0.056)	0.0576 ± 0.0072 (0.0514)
ϕ_i	$0.174^{+0.071}_{-0.17}$ (0.1313)	$0.235^{+0.088}_{-0.23}$ (0.0035)	$0.26^{+0.10}_{-0.24}$ (0.0021)

Table 4. Hilltop quartic model: full parameter means and 68% limits for the addition of the different supernovae datasets to the CMB+DESI combination. The values in parentheses denote the best-fit parameters for this model.

Hilltop octic potential

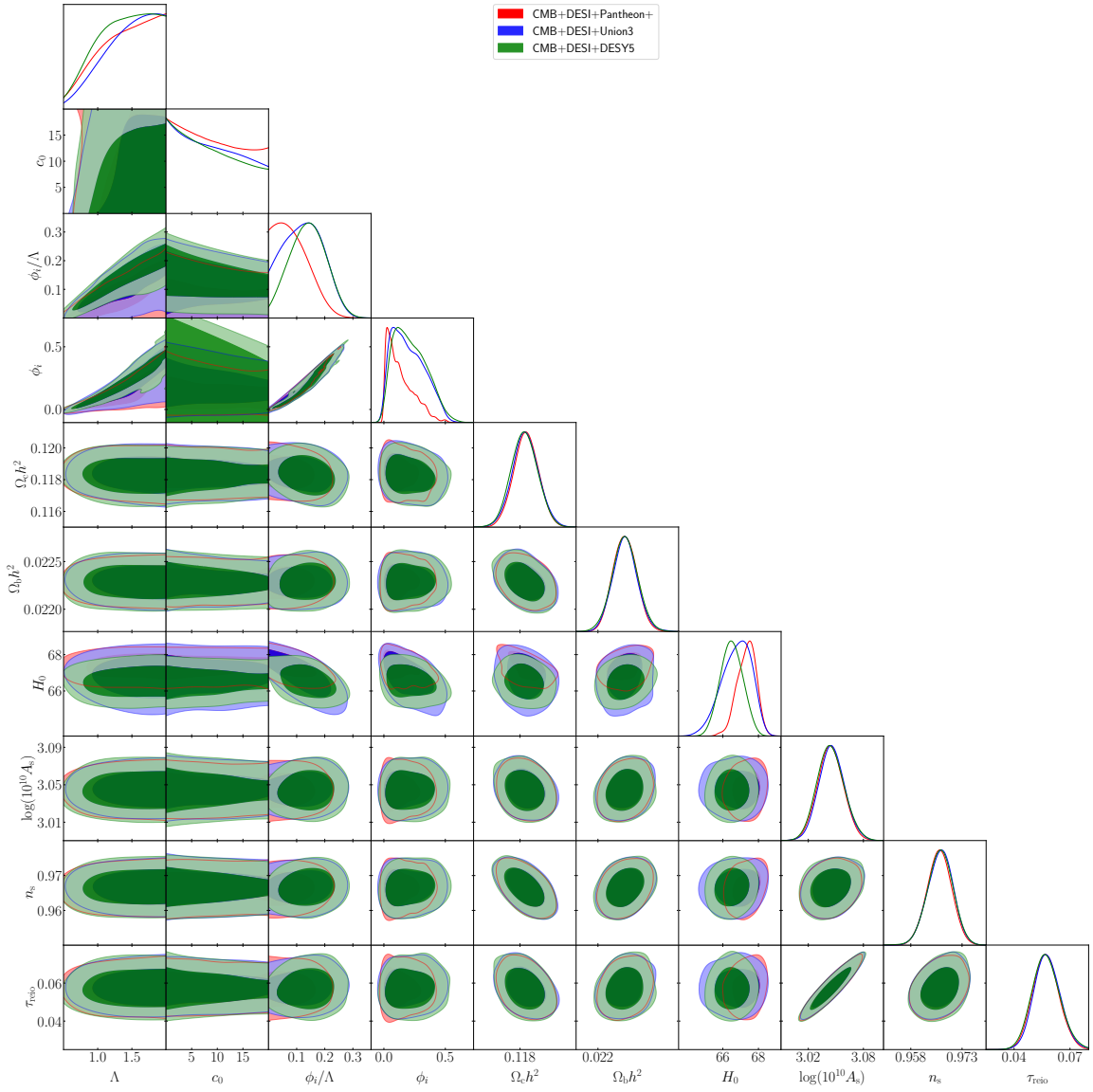

Figure 13. The complete parameter constraints for the hilltop octic model.

Parameter	+Pantheon+	+Union3	+DESY5
$\boldsymbol{\Lambda}$	> 1.21 (0.995)	> 1.29 (1.195)	> 1.18 (0.826)
$\boldsymbol{c_0}$	— (8.91)	< 12.4 (14.27)	< 11.8 (9.78)
$\boldsymbol{\phi_i/\Lambda}$	< 0.113 (0.067)	0.127 ± 0.067 (0.133)	0.141 ± 0.062 (0.071)
$\boldsymbol{\Omega_c h^2}$	0.11839 ± 0.00079 (0.1181)	0.11835 ± 0.00084 (0.1182)	0.11828 ± 0.00084 (0.1178)
$\boldsymbol{\log(10^{10} A_s)}$	3.044 ± 0.014 (3.048)	3.045 ± 0.014 (3.049)	3.044 ± 0.015 (3.048)
$\boldsymbol{n_s}$	0.9664 ± 0.0035 (0.967)	0.9666 ± 0.0036 (0.967)	0.9666 ± 0.0037 (0.967)
$\boldsymbol{H_0}$	$67.34^{+0.59}_{-0.47}$ (67.31)	$66.78^{+0.97}_{-0.70}$ (65.47)	66.50 ± 0.62 (65.87)
$\boldsymbol{\Omega_b h^2}$	0.02229 ± 0.00012 (0.02229)	0.02229 ± 0.00013 (0.02225)	0.02229 ± 0.00014 (0.02228)
$\boldsymbol{\tau_{reio}}$	0.0571 ± 0.0069 (0.0581)	0.0577 ± 0.0069 (0.0589)	$0.0571^{+0.0069}_{-0.0078}$ (0.0595)
ϕ_i	$0.136^{+0.044}_{-0.14}$ (0.067)	$0.199^{+0.091}_{-0.17}$ (0.016)	$0.214^{+0.097}_{-0.17}$ (0.059)

Table 5. Hilltop octic model: full parameter means and 68% limits for the addition of the different supernovae datasets to the CMB+DESI combination. The values in parentheses denote the best-fit parameters for this model.

Hilltop exponential potential

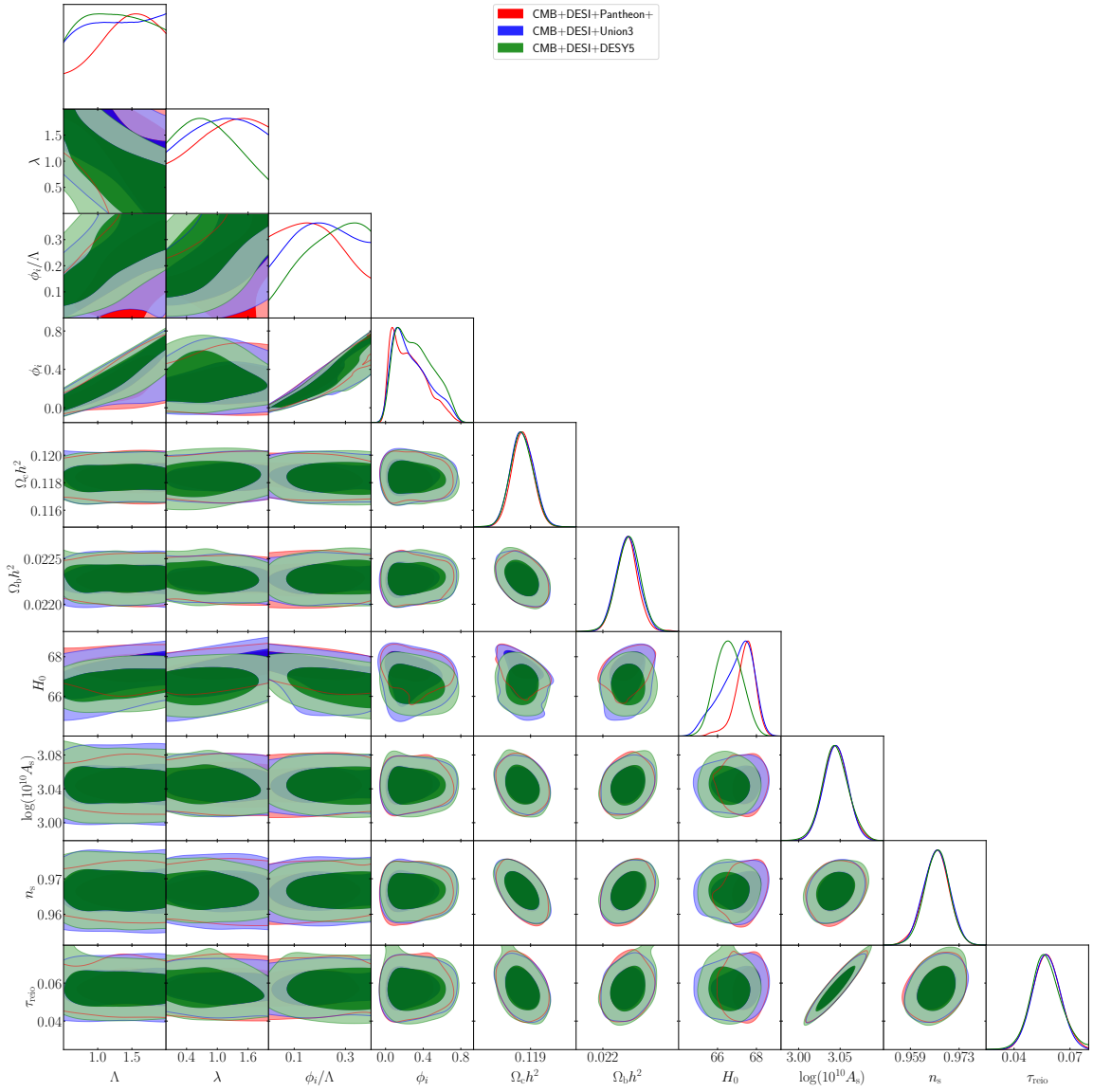

Figure 14. The complete parameter constraints for the hilltop exponential model.

Parameter	+Pantheon+	+Union3	+DESY5
$\boldsymbol{\Lambda}$	$1.36^{+0.64}_{-0.20}$ (0.595)	— (0.742)	— (0.524)
$\boldsymbol{\lambda}$	> 0.823 (1.77)	— (1.76)	$0.89^{+0.36}_{-0.80}$ (1.95)
$\boldsymbol{\phi_i/\Lambda}$	$0.180^{+0.068}_{-0.17}$ (0.243)	0.21 ± 0.11 (0.333)	> 0.183 (0.301)
$\boldsymbol{\Omega_c h^2}$	0.11840 ± 0.00079 (0.1179)	0.11839 ± 0.00085 (0.1179)	0.11835 ± 0.00085 (0.1184)
$\boldsymbol{\log(10^{10} A_s)}$	3.045 ± 0.015 (3.050)	3.045 ± 0.014 (3.046)	3.044 ± 0.016 (3.037)
$\boldsymbol{n_s}$	00.9664 ± 0.0037 (0.968)	0.9665 ± 0.0037 (0.966)	0.9666 ± 0.0036 (0.967)
$\boldsymbol{H_0}$	$67.42^{+0.57}_{-0.39}$ (67.31)	$67.0^{+1.1}_{-0.60}$ (66.04)	66.58 ± 0.67 (66.43)
$\boldsymbol{\Omega_b h^2}$	0.02227 ± 0.00013 (0.02233)	0.02228 ± 0.00013 (0.02234)	0.02229 ± 0.00013 (0.02232)
$\boldsymbol{\tau_{reio}}$	0.0574 ± 0.0075 (0.0607)	0.0573 ± 0.0073 (0.057)	$0.0571^{+0.0073}_{-0.0083}$ (0.0522)
ϕ_i	$0.25^{+0.10}_{-0.23}$ (0.145)	$0.28^{+0.12}_{-0.24}$ (0.247)	$0.31^{+0.14}_{-0.26}$ (0.158)

Table 6. Hilltop exponential model: full parameter means and 68% limits for the addition of the different supernovae datasets to the CMB+DESI combination. The values in parentheses denote the best-fit parameters for this model.

PySR potential

In analyzing this model we only explore the parameter space for the CMB+DESI+Union3 combination. This is because the SR was performed assuming the DESI reconstruction of $w(z)$, which is based on the same data combination. Therefore, applying the same analysis to the CMB+DESI+Pantheon+ and CMB+DESI+DESY5 combinations, as we did for the other models, would be inconclusive.

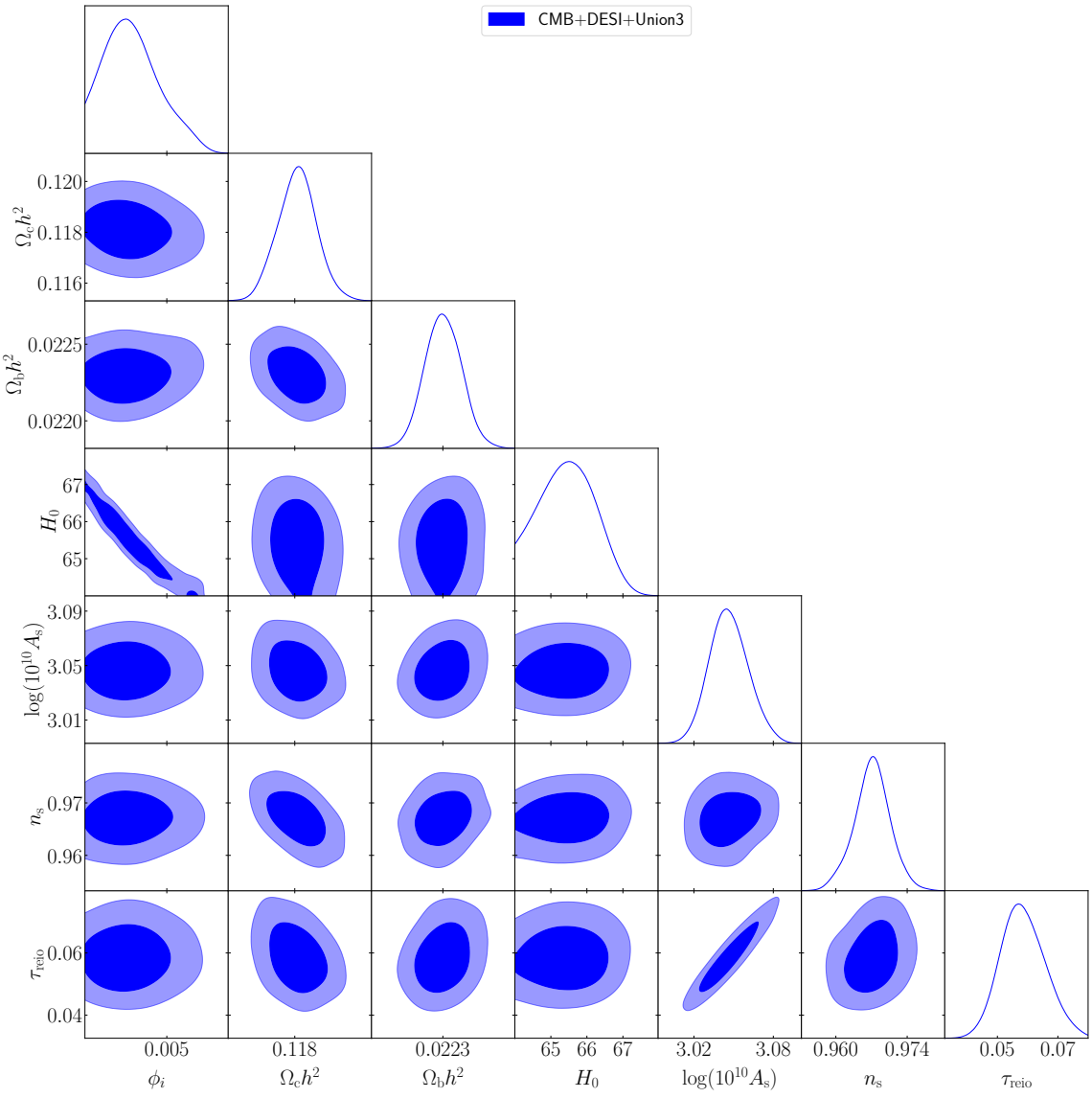

Figure 15. The parameter constraints for the PySR model.

Parameter	+Union3
$\boldsymbol{\Omega_c h^2}$	0.11810 ± 0.00078 (0.1182)
$\boldsymbol{\log(10^{10} A_s)}$	$3.046^{+0.014}_{-0.016}$ (3.042)
$\boldsymbol{n_s}$	0.9671 ± 0.0036 (0.966)
$\boldsymbol{H_0}$	65.48 ± 0.75 (65.04)
$\boldsymbol{\Omega_b h^2}$	0.02230 ± 0.00012 (0.02228)
$\boldsymbol{\tau_{reio}}$	$0.0585^{+0.0068}_{-0.0079}$ (0.0567)
ϕ_i	$0.00377^{+0.00072}_{-0.0013}$ (0.0042)

Table 7. PySR model: parameter means and 68% limits for the CMB+DESI+Union3 combination. The values in parentheses denote the best-fit parameters for this model.

References

[1] S. Weinberg, "The Cosmological Constant Problem," *Rev. Mod. Phys.* **61** (1989) 1–23.

[2] **DES** Collaboration, T. M. C. Abbott *et al.*, "The Dark Energy Survey: Cosmology Results With ˜1500 New High-redshift Type Ia Supernovae Using The Full 5-year Dataset," arXiv:2401.02929 [astro-ph.CO].

[3] **DESI** Collaboration, A. G. Adame *et al.*, "DESI 2024 VI: Cosmological Constraints from the Measurements of Baryon Acoustic Oscillations," arXiv:2404.03002 [astro-ph.CO].

[4] **DESI** Collaboration, A. G. Adame *et al.*, "DESI 2024 VII: Cosmological Constraints from the Full-Shape Modeling of Clustering Measurements," arXiv:2411.12022 [astro-ph.CO].

[5] **DES** Collaboration, T. M. C. Abbott *et al.*, "Dark Energy Survey: implications for cosmological expansion models from the final DES Baryon Acoustic Oscillation and Supernova data," arXiv:2503.06712 [astro-ph.CO].

[6] E. O. Colgáin, M. G. Dainotti, S. Capozziello, S. Pourojaghi, M. M. Sheikh-Jabbari, and D. Stojkovic, "Does DESI 2024 Confirm ΛCDM?," arXiv:2404.08633 [astro-ph.CO].

[7] Y. Carloni, O. Luongo, and M. Muccino, "Does dark energy really revive using DESI 2024 data?," arXiv:2404.12068 [astro-ph.CO].

[8] C.-G. Park, J. de Cruz Perez, and B. Ratra, "Using non-DESI data to confirm and strengthen the DESI 2024 spatially-flat w_0w_aCDM cosmological parameterization result," arXiv:2405.00502 [astro-ph.CO].

[9] D. Wang, "The Self-Consistency of DESI Analysis and Comment on "Does DESI 2024 Confirm ΛCDM?"," arXiv:2404.13833 [astro-ph.CO].

[10] M. Cortês and A. R. Liddle, "Interpreting DESI's evidence for evolving dark energy," arXiv:2404.08056 [astro-ph.CO].

[11] Z. Wang, S. Lin, Z. Ding, and B. Hu, "The role of LRG1 and LRG2's monopole in inferring the DESI 2024 BAO cosmology," arXiv:2405.02168 [astro-ph.CO].

[12] B. R. Dinda, "A new diagnostic for the null test of dynamical dark energy in light of DESI 2024 and other BAO data," arXiv:2405.06618 [astro-ph.CO].

[13] K. S. Croker, G. Tarlé, S. P. Ahlen, B. G. Cartwright, D. Farrah, N. Fernandez, and R. A. Windhorst, "DESI Dark Energy Time Evolution is Recovered by Cosmologically Coupled Black Holes," arXiv:2405.12282 [astro-ph.CO].

[14] D. Wang, "Constraining Cosmological Physics with DESI BAO Observations," arXiv:2404.06796 [astro-ph.CO].

[15] O. Luongo and M. Muccino, "Model independent cosmographic constraints from DESI 2024," arXiv:2404.07070 [astro-ph.CO].

[16] P. Mukherjee and A. A. Sen, "Model-independent cosmological inference post DESI DR1 BAO measurements," arXiv:2405.19178 [astro-ph.CO].

[17] H. Wang and Y.-S. Piao, "Dark energy in light of recent DESI BAO and Hubble tension," arXiv:2404.18579 [astro-ph.CO].

[18] G. Efstathiou, "Evolving Dark Energy or Supernovae Systematics?," arXiv:2408.07175 [astro-ph.CO].

[19] Y. Tada and T. Terada, "Quintessential interpretation of the evolving dark energy in light of DESI observations," *Phys. Rev. D* **109** no. 12, (2024) L121305, arXiv:2404.05722 [astro-ph.CO].

[20] W. Yin, "Cosmic Clues: DESI, Dark Energy, and the Cosmological Constant Problem," arXiv:2404.06444 [hep-ph].

[21] K. V. Berghaus, J. A. Kable, and V. Miranda, "Quantifying Scalar Field Dynamics with DESI 2024 Y1 BAO measurements," arXiv:2404.14341 [astro-ph.CO].

[22] D. Shlivko and P. J. Steinhardt, "Assessing observational constraints on dark energy," *Phys. Lett. B* **855** (2024) 138826, arXiv:2405.03933 [astro-ph.CO].

[23] G. Alestas, M. Caldarola, S. Kuroyanagi, and S. Nesseris, "DESI constraints on α-attractor inflationary models," arXiv:2410.00827 [astro-ph.CO].

[24] S. Sohail, S. Alam, S. Akthar, and M. W. Hossain, "Quintessential early dark energy," arXiv:2408.03229 [astro-ph.CO].

[25] S. Roy Choudhury and T. Okumura, "Updated Cosmological Constraints in Extended Parameter Space with Planck PR4, DESI Baryon Acoustic Oscillations, and Supernovae: Dynamical Dark Energy, Neutrino Masses, Lensing Anomaly, and the Hubble Tension," *Astrophys. J. Lett.* **976** no. 1, (2024) L11, arXiv:2409.13022 [astro-ph.CO].

[26] W. Giarè, M. Najafi, S. Pan, E. Di Valentino, and J. T. Firouzjaee, "Robust preference for Dynamical Dark Energy in DESI BAO and SN measurements," *JCAP* **10** (2024) 035, arXiv:2407.16689 [astro-ph.CO].

[27] W. Giarè, M. A. Sabogal, R. C. Nunes, and E. Di Valentino, "Interacting Dark Energy after DESI Baryon Acoustic Oscillation Measurements," *Phys. Rev. Lett.* **133** no. 25, (2024) 251003, arXiv:2404.15232 [astro-ph.CO].

[28] W. Giarè, "Dynamical Dark Energy Beyond Planck? Constraints from multiple CMB probes, DESI BAO and Type-Ia Supernovae," arXiv:2409.17074 [astro-ph.CO].

[29] W. Giarè, T. Mahassen, E. Di Valentino, and S. Pan, "An overview of what current data can (and cannot yet) say about evolving dark energy," arXiv:2502.10264 [astro-ph.CO].

[30] R. E. Keeley, K. N. Abazajian, M. Kaplinghat, and A. Shafieloo, "The Preference for Evolving Dark Energy from Cosmological Distance Measurements and Possible Signatures in the Growth Rate of Perturbations," arXiv:2502.12667 [astro-ph.CO].

[31] **DES** Collaboration, M. Vincenzi *et al.*, "Comparing the DES-SN5YR and Pantheon+ SN cosmology analyses: Investigation based on "Evolving Dark Energy or Supernovae systematics?"," arXiv:2501.06664 [astro-ph.CO].

[32] C.-G. Park and B. Ratra, "Is excess smoothing of Planck CMB ansiotropy data partially responsible for evidence for dark energy dynamics in other $w(z)$CDM parametrizations?," arXiv:2501.03480 [astro-ph.CO].

[33] S. S. Taylor and R. J. Scherrer, "What do we learn by mapping dark energy to a single value of w?," *Phys. Rev. D* **111** no. 4, (2025) 043534, arXiv:2412.08766 [astro-ph.CO].

[34] E. O. Colgáin and M. M. Sheikh-Jabbari, "DESI and SNe: Dynamical Dark Energy, Ω_m Tension or Systematics?," arXiv:2412.12905 [astro-ph.CO].

[35] G. Payeur, E. McDonough, and R. Brandenberger, "Do Observations Prefer Thawing Quintessence?," arXiv:2411.13637 [astro-ph.CO].

[36] M. Berbig, "Kick it like DESI: PNGB quintessence with a dynamically generated initial velocity," *JCAP* **03** (2025) 015, arXiv:2412.07418 [astro-ph.CO].

[37] D. Sapone and S. Nesseris, "Outliers in DESI BAO: robustness and cosmological implications," arXiv:2412.01740 [astro-ph.CO].

[38] Q. Gao, Z. Peng, S. Gao, and Y. Gong, "On the Evidence of Dynamical Dark Energy," *Universe* **11** no. 1, (2025) 10, arXiv:2411.16046 [astro-ph.CO].

[39] D. Tamayo, E. Urquilla, and I. Gómez-Vargas, "Equivalence of Dark Energy Models: A Theoretical and Bayesian Perspective," arXiv:2502.12915 [astro-ph.CO].

[40] A. N. Ormondroyd, W. J. Handley, M. P. Hobson, and A. N. Lasenby, "Nonparametric reconstructions of dynamical dark energy via flexknots," arXiv:2503.08658 [astro-ph.CO].

[41] M. Chevallier and D. Polarski, "Accelerating universes with scaling dark matter," *Int. J. Mod. Phys. D* **10** (2001) 213–224, arXiv:gr-qc/0009008.

[42] E. V. Linder, "Exploring the expansion history of the universe," *Phys. Rev. Lett.* **90** (2003)

091301, arXiv:astro-ph/0208512.

[43] B. Ratra and P. J. E. Peebles, "Cosmological Consequences of a Rolling Homogeneous Scalar Field," *Phys. Rev. D* **37** (1988) 3406.

[44] R. R. Caldwell, R. Dave, and P. J. Steinhardt, "Cosmological imprint of an energy component with general equation of state," *Phys. Rev. Lett.* **80** (1998) 1582–1585, arXiv:astro-ph/9708069.

[45] J. A. Frieman, C. T. Hill, A. Stebbins, and I. Waga, "Cosmology with ultralight pseudo Nambu-Goldstone bosons," *Phys. Rev. Lett.* **75** (1995) 2077–2080, arXiv:astro-ph/9505060.

[46] R. R. Caldwell and E. V. Linder, "The Limits of quintessence," *Phys. Rev. Lett.* **95** (2005) 141301, arXiv:astro-ph/0505494.

[47] S. Bhattacharya, G. Borghetto, A. Malhotra, S. Parameswaran, G. Tasinato, and I. Zavala, "Cosmological constraints on curved quintessence," *JCAP* **09** (2024) 073, arXiv:2405.17396 [astro-ph.CO].

[48] S. Bhattacharya, G. Borghetto, A. Malhotra, S. Parameswaran, G. Tasinato, and I. Zavala, "Cosmological tests of quintessence in quantum gravity," arXiv:2410.21243 [astro-ph.CO].

[49] S. Dutta and R. J. Scherrer, "Hilltop Quintessence," *Phys. Rev. D* **78** (2008) 123525, arXiv:0809.4441 [astro-ph].

[50] I. D. Gialamas, G. Hütsi, K. Kannike, A. Racioppi, M. Raidal, M. Vasar, and H. Veermäe, "Interpreting DESI 2024 BAO: late-time dynamical dark energy or a local effect?," arXiv:2406.07533 [astro-ph.CO].

[51] A. Notari, M. Redi, and A. Tesi, "Consistent Theories for the DESI dark energy fit," arXiv:2406.08459 [astro-ph.CO].

[52] C. Cheung and I. Z. Rothstein, "New Physics Hiding at the Ends," arXiv:2411.07380 [hep-ph].

[53] J. McNamara and C. Vafa, "Cobordism Classes and the Swampland," arXiv:1909.10355 [hep-th].

[54] M. Montero and C. Vafa, "Cobordism Conjecture, Anomalies, and the String Lamppost Principle," *JHEP* **01** (2021) 063, arXiv:2008.11729 [hep-th].

[55] R. Blumenhagen, C. Kneissl, and C. Wang, "Dynamical Cobordism Conjecture: solutions for end-of-the-world branes," *JHEP* **05** (2023) 123, arXiv:2303.03423 [hep-th].

[56] G. Buratti, J. Calderón-Infante, M. Delgado, and A. M. Uranga, "Dynamical Cobordism and Swampland Distance Conjectures," *JHEP* **10** (2021) 037, arXiv:2107.09098 [hep-th].

[57] K. Hinterbichler and J. Khoury, "Symmetron Fields: Screening Long-Range Forces Through Local Symmetry Restoration," *Phys. Rev. Lett.* **104** (2010) 231301,

arXiv:1001.4525 [hep-th].

[58] I. Antoniadis, Y. Chen, and G. K. Leontaris, "Logarithmic loop corrections, moduli stabilisation and de Sitter vacua in string theory," *JHEP* **01** (2020) 149, arXiv:1909.10525 [hep-th].

[59] S. K. Garg and C. Krishnan, "Bounds on Slow Roll and the de Sitter Swampland," *JHEP* **11** (2019) 075, arXiv:1807.05193 [hep-th].

[60] H. Ooguri, E. Palti, G. Shiu, and C. Vafa, "Distance and de Sitter Conjectures on the Swampland," *Phys. Lett. B* **788** (2019) 180–184, arXiv:1810.05506 [hep-th].

[61] Y. Olguin-Trejo, S. L. Parameswaran, G. Tasinato, and I. Zavala, "Runaway Quintessence, Out of the Swampland," *JCAP* **01** (2019) 031, arXiv:1810.08634 [hep-th].

[62] L. McAllister, E. Silverstein, and A. Westphal, "Gravity Waves and Linear Inflation from Axion Monodromy," *Phys. Rev. D* **82** (2010) 046003, arXiv:0808.0706 [hep-th].

[63] A. Lewis, A. Challinor, and A. Lasenby, "Efficient computation of CMB anisotropies in closed FRW models," *Astrophys. J.* **538** (2000) 473–476, arXiv:astro-ph/9911177 [astro-ph]. https://arxiv.org/abs/astro-ph/9911177.

[64] **Planck** Collaboration, N. Aghanim *et al.*, "Planck 2018 results. V. CMB power spectra and likelihoods," *Astron. Astrophys.* **641** (2020) A5, arXiv:1907.12875 [astro-ph.CO].

[65] E. Rosenberg, S. Gratton, and G. Efstathiou, "CMB power spectra and cosmological parameters from Planck PR4 with CamSpec," *Mon. Not. Roy. Astron. Soc.* **517** no. 3, (2022) 4620–4636, arXiv:2205.10869 [astro-ph.CO].

[66] **Planck** Collaboration, N. Aghanim *et al.*, "Planck 2018 results. VIII. Gravitational lensing," *Astron. Astrophys.* **641** (2020) A8, arXiv:1807.06210 [astro-ph.CO].

[67] **DESI** Collaboration, A. G. Adame *et al.*, "DESI 2024 IV: Baryon Acoustic Oscillations from the Lyman Alpha Forest," arXiv:2404.03001 [astro-ph.CO].

[68] **DESI** Collaboration, A. G. Adame *et al.*, "DESI 2024 III: Baryon Acoustic Oscillations from Galaxies and Quasars," arXiv:2404.03000 [astro-ph.CO].

[69] D. Brout *et al.*, "The Pantheon+ Analysis: Cosmological Constraints," *Astrophys. J.* **938** no. 2, (2022) 110, arXiv:2202.04077 [astro-ph.CO].

[70] D. Rubin *et al.*, "Union Through UNITY: Cosmology with 2,000 SNe Using a Unified Bayesian Framework," arXiv:2311.12098 [astro-ph.CO].

[71] A. Lewis and S. Bridle, "Cosmological parameters from CMB and other data: A Monte Carlo approach," *Phys. Rev.* **D66** (2002) 103511, arXiv:astro-ph/0205436 [astro-ph]. https://arxiv.org/abs/astro-ph/0205436.

[72] A. Lewis, "Efficient sampling of fast and slow cosmological parameters," *Phys. Rev.* **D87** no. 10, (2013) 103529, arXiv:1304.4473 [astro-ph.CO]. https://arxiv.org/abs/1304.4473.

[73] J. Torrado and A. Lewis, "Cobaya: Code for Bayesian Analysis of hierarchical physical

models," *JCAP* **05** (2021) 057, arXiv:2005.05290 [astro-ph.IM].

[74] A. Lewis, "GetDist: a Python package for analysing Monte Carlo samples," arXiv:1910.13970 [astro-ph.IM].

[75] P. Virtanen, R. Gommers, T. E. Oliphant, M. Haberland, T. Reddy, D. Cournapeau, E. Burovski, P. Peterson, W. Weckesser, J. Bright, S. J. van der Walt, M. Brett, J. Wilson, K. J. Millman, N. Mayorov, A. R. J. Nelson, E. Jones, R. Kern, E. Larson, C. J. Carey, İ. Polat, Y. Feng, E. W. Moore, J. VanderPlas, D. Laxalde, J. Perktold, R. Cimrman, I. Henriksen, E. A. Quintero, C. R. Harris, A. M. Archibald, A. H. Ribeiro, F. Pedregosa, P. van Mulbregt, and SciPy 1.0 Contributors, "SciPy 1.0: Fundamental Algorithms for Scientific Computing in Python," *Nature Methods* **17** (2020) 261–272.

[76] R. Calderon *et al.*, "DESI 2024: Reconstructing Dark Energy using Crossing Statistics with DESI DR1 BAO data," arXiv:2405.04216 [astro-ph.CO].

[77] T. Sousa, D. J. Bartlett, H. Desmond, and P. G. Ferreira, "Optimal inflationary potentials," *Phys. Rev. D* **109** no. 8, (2024) 083524, arXiv:2310.16786 [astro-ph.CO].

[78] A. Sousa-Neto, C. Bengaly, J. E. González, and J. Alcaniz, "No evidence for dynamical dark energy from DESI and SN data: a symbolic regression analysis," arXiv:2502.10506 [astro-ph.CO].

[79] M. Cranmer, "Interpretable machine learning for science with pysr and symbolicregression.jl," 2023. https://arxiv.org/abs/2305.01582.